

# Temperature dependent crack initiation of 42CrMo4 steel at high loading rates

Sebastian Henschel<sup>1,\*</sup> and Lutz Krüger<sup>1</sup>

<sup>1</sup>Institute of Materials Engineering, TU Bergakademie Freiberg, Gustav-Zeuner-Str. 5, 09599 Freiberg, Germany

**Abstract.** Dynamic crack initiation with crack tip loading rates  $\dot{K}$  of approximately  $2 \cdot 10^6$  MPa  $\sqrt{\text{m}} \text{ s}^{-1}$  in high-strength 42CrMo4 steel was investigated. To this end, a recently developed split Hopkinson pressure bar with four-point bending was utilized. V-notched and precracked Charpy specimens were tested. The tests were performed at temperatures of  $-40$  °C and  $20$  °C. The loading of the specimen was determined by analyzing the strain in the incident and transmission bars. Furthermore, strain gauges at the specimen's surface were applied to measure the crack tip loading. High-speed photography complemented the analysis of the specimens loading and the detection of the crack initiation. Fracture surface analysis by means of scanning electron microscopy enabled the measurement of the fracture surface topography and, consequently, stretch zone height and width. Hence, the macroscopically measured dynamic crack initiation toughness was correlated with the toughness at microscopic scale. It was observed that the resistance against dynamic crack initiation decreased with decreasing temperature. Microscopically, a decrease in toughness was analogously observed. Non-metallic inclusions resulted in crack path deflection with localized shear zones. After a small stable crack extension, cleavage fracture was observed.

## 1 Introduction

The dynamic fracture toughness behavior of different materials can be studied by utilizing the split Hopkinson pressure bar (SHPB) [1]. Both the incident and the transmission bars are used to analyze forces and displacements. Hence, the dynamic force equilibrium between loading and support faces of the specimen can be evaluated [2, 3].

Pulse shaping is applied to increase the rise time of the originally rectangular pulse generated by the impact of the striker bar to the incident bar. Hence, the frequency spectrum of the incident pulse is limited [4, 5].

Ductile fracture consists of void nucleation, void growth and coalescence and is strongly affected by non-metallic inclusions. It is known that elongated inclusions, e. g. MnS, or agglomerated inclusions, e. g.  $\text{Al}_2\text{O}_3$ , serve as favorable void nucleation sites [6]. Hence, the growing crack interacts with the voids and will be deflected towards these voids [7].

Investigations of Klepaczko [8, 9] showed that there is a minimum plane-strain fracture toughness at  $\dot{K} \approx 10^4$  MPa  $\sqrt{\text{m}} \text{ s}^{-1}$  for a C45 steel. Own studies [10, 11] do not show a minimum of the toughness at intermediate loading rates of  $10^4$  to  $10^5$  MPa  $\sqrt{\text{m}} \text{ s}^{-1}$ . Furthermore, pronounced scatter is observed at high loading rates of  $2 \cdot 10^6$  MPa  $\sqrt{\text{m}} \text{ s}^{-1}$ . Throughout the loading rate spectrum no cleavage fracture was observed when testing at ambient temperature.

Krabiell and Dahl [12] studied the effect of temperature and loading rate on the fracture toughness behavior of different structural steels. They observed a slight loading

rate dependency of the upper shelf toughness. The fracture toughness increased with increasing loading rate. In contrast, within the temperature range of the ductile-to-brittle transition, an increase in loading rate resulted in a pronounced decrease in fracture toughness.

The strain field around the crack tip can be analyzed by strain gauges. Since the strain near the crack tip is proportional to  $K_I$  at low loads, a direct load ( $F$  or  $K_I$ ) measurement is achieved [13]. Furthermore, the point of crack initiation can be detected with such a strain gauge [14].

The aim of this study is to investigate the temperature effect on the fracture toughness behavior at high loading rates of  $2 \cdot 10^6$  MPa  $\sqrt{\text{m}} \text{ s}^{-1}$ . To this end, a split Hopkinson pressure bar was equipped with a chamber which allows to cool the specimen while keeping the possibility to perform high-speed photography. The loading of the specimen was analyzed by the force measurement at the bars and by strain gauges at the specimen.

## 2 Materials and Methods

### 2.1 Investigated steel

The resistance to crack initiation, i. e. the onset of crack growth, of the hot-rolled steel 42CrMo4 (1.7225) was investigated. The steel was tested in the quenched and tempered condition. Quenching consisted of austenitizing at  $840$  °C for 20 min in vacuum and quenching in a stream of He. Tempering was conducted at  $560$  °C for 60 min in  $\text{N}_2$  atmosphere. Consequently, the microstructure consisted of tempered martensite.

Notched and heat-treated specimens were fatigued to introduce a precrack with  $a_0/W \approx 0.5$ . The precracking

\*e-mail: [sebastian.henschel@iwt.tu-freiberg.de](mailto:sebastian.henschel@iwt.tu-freiberg.de)

was started with  $\Delta K = 18 \text{ MPa}\sqrt{\text{m}}$  at a stress ratio of  $R = 0.1$ . The load was reduced in four steps to obtain a crack tip with a minimized plastic zone. This process was controlled by the crack length dependent resonant frequency.

## 2.2 Experimental setup

Figure 1 shows a schematic of the used split Hopkinson pressure bar. The bars were made of high strength AA7075 wrought aluminum alloy. Both incident and transmission bars had a common cross sectional area ( $707 \text{ mm}^2$ ). The striker bar was propelled by compressed air to  $v_S \approx 9.9 \text{ m/s}$ . Further details of the setup are described elsewhere [11].

The specimens were instrumented with strain gauges (SG), see Figure 2. Two SG were located at the outer fiber of the specimen. These strain gauges enabled the direct measurement of the specimen loading, i. e. the force  $F_{\text{Specimen}}$ . The principle of the force measurement described in ASTM E 1820 [15] was adopted. Since four-point bending was applied, it was not possible to attach strain gauges to the opposite surface of the specimen, see Figure 2. Hence, only two strain gauges were used to measure the outer fiber strain of the beam. These strain gauges were calibrated statically. The other SG was positioned near the crack tip ( $r = 5 \text{ mm}$ ). This strain gauge was applied to indicate the specimen loading and the onset of crack growth. A static calibration at low loads ( $K \leq 20 \text{ MPa}\sqrt{\text{m}}$ ) was performed to obtain  $F_{\text{Crack}}$ .

The high-speed camera Photron FASTCAM SA-Z was utilized to capture the development of the plastic zone and the crack opening at the surface of the specimen. A frame rate of 330,000 fps in combination with an image size of  $384 \times 96$  pixels was applied.

The specimen was cooled to the desired temperature at the final position in the machine. Cooling in an external medium was not possible since the positioning between the loading and support pins takes much longer than 5 s. However shorter times for positioning of the specimen are required, e. g. by DIN EN ISO 148-1 [16]. Consequently, cool gaseous nitrogen was used to cool down the specimen in a small chamber. The temperature of the specimen was measured by a thermocouple welded to the specimen. Due to the necessity to handle the specimen within the chamber, also some parts of the incident and transmission bars are in the cooling chamber. Hence, these bars were also cooled to some extent.

During cooling, the chamber consists of several plates made of fiber-reinforced plastic (trade name pertinax). One plate can be quickly replaced by a transparent polymethyl methacrylate (PMMA) plate. Consequently, high-speed photography was possible. The heating of the specimen was minimized by applying LED spotlights. However, the test has to be performed just after turning the lights on to prevent the specimen from unwanted heating. Furthermore, the flow of gaseous nitrogen has to be stopped in order to enhance the visibility of the specimen.

## 2.3 Data analysis

Since the bars only deform elastically, the forces in the bars are calculated by strain measurement at the surface of the bars, see Figure 1:

$$F_1(t) = F_I(t) + F_R(t) = \frac{\pi}{4} d^2 E_B (\varepsilon_I(t) + \varepsilon_R(t)) \quad (1)$$

$$F_2(t) = F_T(t) = \frac{\pi}{4} (d_o^2 - d_i^2) E_B \varepsilon_T(t) \quad (2)$$

$$z_1(t) = c_B \int_0^t (\varepsilon_I(t') + \varepsilon_R(t')) dt' \quad (3)$$

$$z_2(t) = c_B \int_0^t \varepsilon_T(t') dt' \quad (4)$$

The modulus of elasticity of the bars  $E_B = 72389 \text{ MPa}$  was determined by ultrasonic methods. Additional to the strain gauges, a laser system (Polytec OFV-525) was utilized to measure the surface velocity, and, consequently, calculate the strain by [17]:

$$\varepsilon = v_B / c_B \quad (5)$$

here,  $v_B$  is the surface velocity of the bar, and  $c_B$  is the sound velocity of the bar material. The applicability of the laser based measurement of was verified in a previous study [18].

Force equilibrium was achieved when  $F_1(t) = F_2(t)$ , i. e.  $\varepsilon_I(t) + \varepsilon_R(t) = \varepsilon_T(t)$ . Hence, the relative displacement of the loading pins was then given by:

$$\delta(t) = z_1(t) - z_2(t) = -2c_B \int_0^t \varepsilon_R(t') dt' \quad (6)$$

In previous investigations [18], it was observed that after achieving force equilibrium, quasi-static relationships between measured forces, stress intensity factor and J integral are valid.

## 2.4 Calculation of the J integral

Under the assumption of quasi-static conditions, the J integral at the point of crack initiation was determined according to ISO 26843 [14]:

$$J = \frac{K^2(1 - \nu^2)}{E} + \frac{2U_p}{B_N(W - a_0)} \quad (7)$$

The quasi-static stress intensity factor  $K_1^{\text{stat}}$  was calculated for the four-point bend loading according to ASTM C 1421 [19]:

$$K_1^{\text{stat}} = \frac{F(S_o - S_i)}{BW^{3/2}} \cdot \frac{3(a_0/W)^{1/2}}{2(1 - a_0/W)^{3/2}} \cdot f(a_0/W) \quad (8)$$

The plastic part of the energy  $U_p$  was determined from the force-displacement curve. During force equilibrium,  $F_1$  and  $F_2$  can be used to calculate  $K_1^{\text{stat}}$  and  $U_p$ .

## 2.5 Fractography

Scanning electron microscopy (SEM) was applied to analyze the fracture surfaces. The SEM MIRA 3 XMU (TESCAN) was utilized to measure the fracture surface topography by beam tilting or sample tilting. The capabilities of this technique are described elsewhere [20].

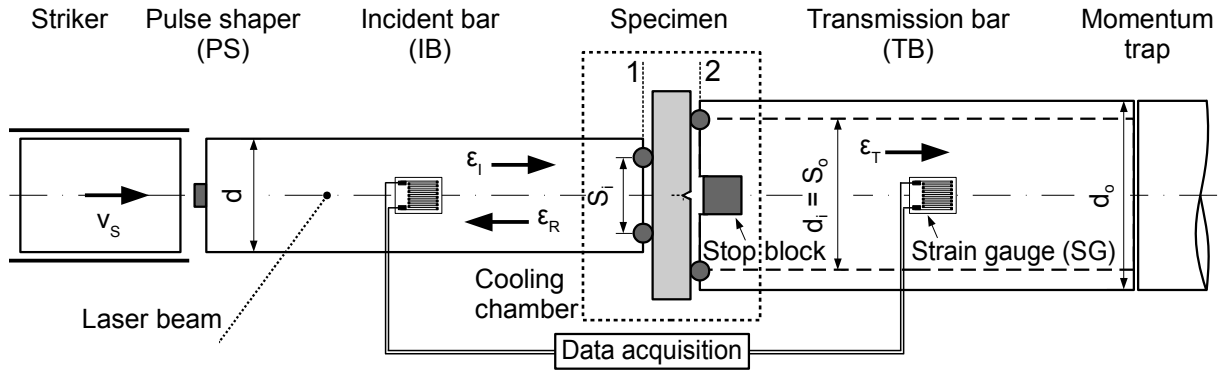


**Fig. 1.** Setup of the four-point bending split Hopkinson pressure bar. Diameters  $d = 30$  mm and  $d_0 = 50$  mm, inner span  $S_1 = 20$  mm, outer span  $S_0 = 40$  mm. Pulse shaper: pure copper, diameter 5 mm, thickness 0.5 mm.

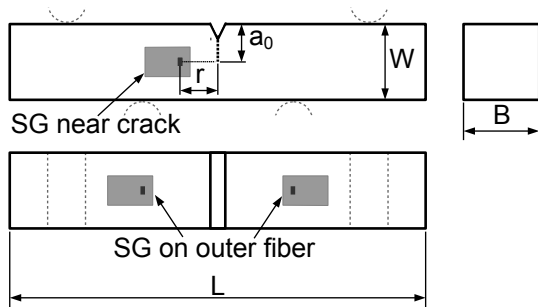


**Fig. 2.** Position of the strain gauges on the specimen ( $B \times W \times L = 10 \times 10 \times 55$  mm<sup>3</sup>).

### 3 Results and Discussion

#### 3.1 Temperature dependent specimen response

Figure 3a shows the strains  $\epsilon_I$ ,  $\epsilon_R$  and  $\epsilon_T$ . Thanks to the pulse shaper, the incident pulse has a smooth rise. In Figure 3b, the forces  $F_1$  and  $F_2$  in the incident and transmission bars indicate a force equilibrium up to the onset of stable crack growth. Furthermore, the force measured by the strain gauges at the outer fiber of the specimen ( $F_{\text{Specimen}}$ ) was equal to  $F_1$  and  $F_2$ . After the onset of stable crack growth, there was no force equilibrium.

Figure 4 shows the signals of the strain gauge attached near the crack tip and the corresponding images of the high-speed camera. At low loads, the signal of the strain gauge near the crack tip is proportional to the acting force. The calibration factor was determined statically ( $\approx 6.5$  kN/V). Hence, this strain gauge can also be applied as a load cell additionally to the strain gauges at the outer fiber of the specimen. Consequently, the force equilibrium at low loads was confirmed, see Figure 4. At higher loads, i. e. after the onset of crack extension, the calibration of this strain gauge is not valid anymore. The onset of crack extension was detected by a sudden drop of the strain gauge signal. The drop was caused by the increasing compliance with increasing crack length. A detailed discussion was presented in previous studies [11, 18].

The opening displacement of the crack and the development of the plastic zone was analyzed by applying high-

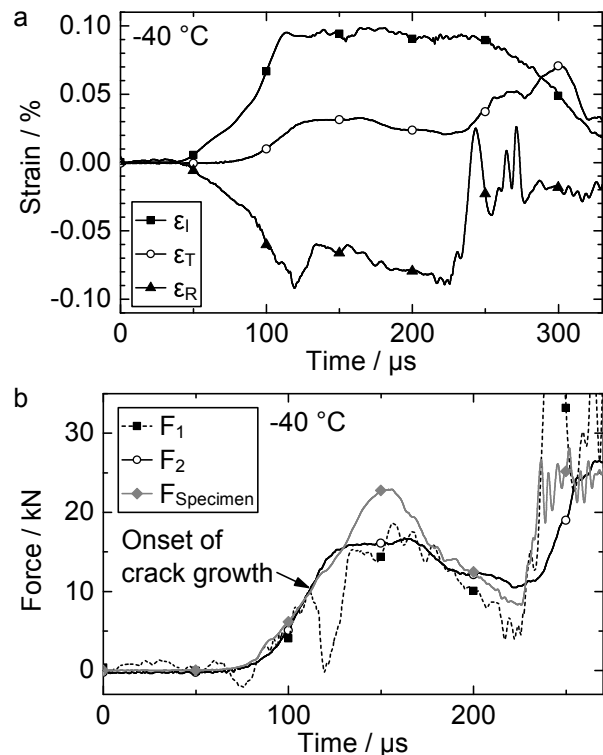


**Fig. 3.** (a) Original strain signals, (b) Calculated forces  $F_1$  and  $F_2$  indicate force equilibrium before onset of stable fracture.  $F_{\text{Specimen}}$  measured by strain gauges at the outer fiber of the specimen.

speed photography, see Figure 4. It was observed that the opening displacement of the crack exhibits a distinct increase in slope at the same time at which the strain gauge near the crack tip indicates the onset of crack extension. Furthermore, the size of the plastic zone strongly increased at this time. This was explained by the crack extension starting in the center of the specimen due to the higher stress triaxiality. At the surface of the specimen, the crack growth is retarded. However, the plastic zone increases.

Figure 5 shows the effect of temperature on the J integral at the onset of stable crack growth. It was found that a decreasing temperature leads to a reduced resistance to

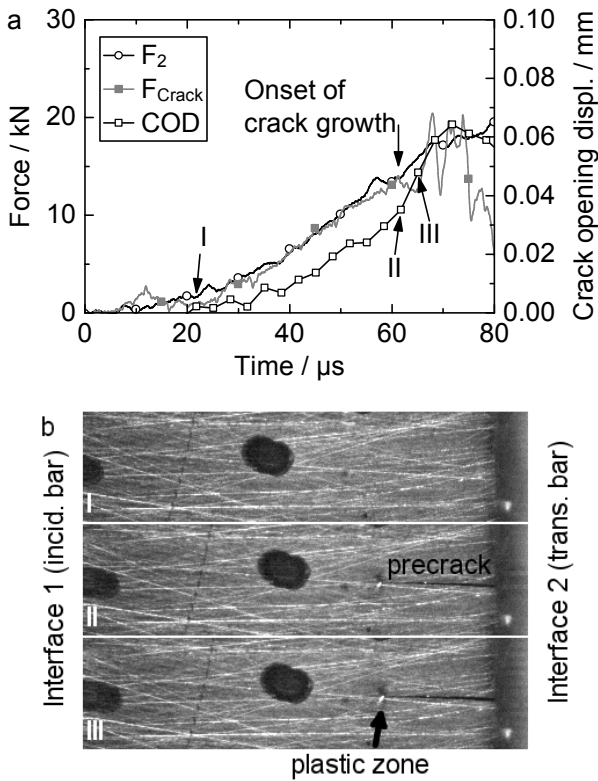


**Fig. 4.** (a) Signal of the strain gauges near the crack tip, (b) crack opening captured by the high-speed camera. The black dots support the positioning of the high-speed camera since the original crack tip has a weak visibility.

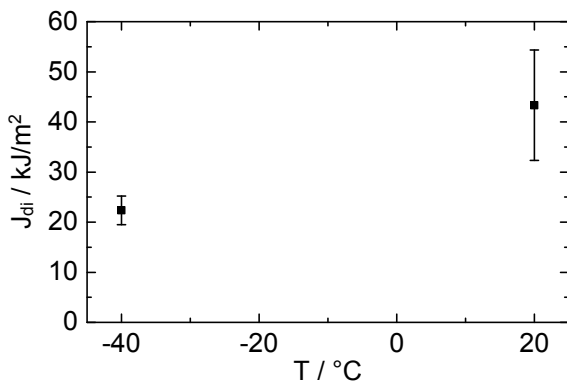


**Fig. 5.** Temperature dependent J integral at the onset of stable crack growth ( $J_{dti}$ ).

crack initiation. The reduction was about 50%. The lower scatter at  $T = -40^\circ\text{C}$  was considered to be not typical for this steel. For many steels, which show a ductile-to-brittle transition, the scatter of the fracture toughness within the range of the transition is considerably larger than at the upper or lower shelf.

### 3.2 Crack tip blunting

Figure 6 shows typical fracture surfaces of specimens tested at  $20^\circ\text{C}$  and  $-40^\circ\text{C}$ . Before the onset of stable crack growth, the fatigue precrack blunted irrespective of

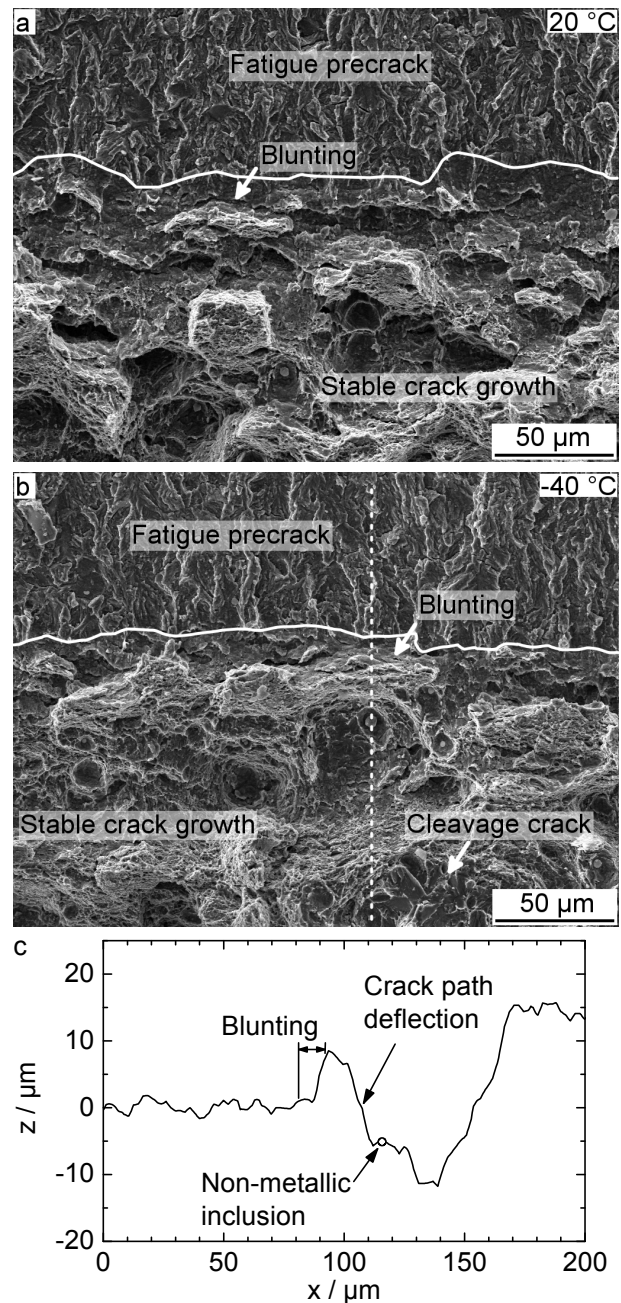


**Fig. 6.** Fracture surfaces showing the features of crack initiation at  $20^\circ\text{C}$  (a) and  $-40^\circ\text{C}$  (b). (c) Height profile for the path in subfigure b.

the temperature. Cleavage crack initiation by non-metallic inclusions without blunting was not observed. However, after a small amount of ductile fracture, unstable crack growth by cleavage cracking was found.

The fracture surface in Figure 6b exhibits non-metallic inclusions. Such inclusions lead to substantial crack path deflection if they were not located in the ideal crack plane. Figure 6c shows the resulting crack path deflection. The corresponding path of this height profile is given in Figure 6b. The crack path deflection was achieved by shear localization and, hence, adiabatic heating. Consequently,

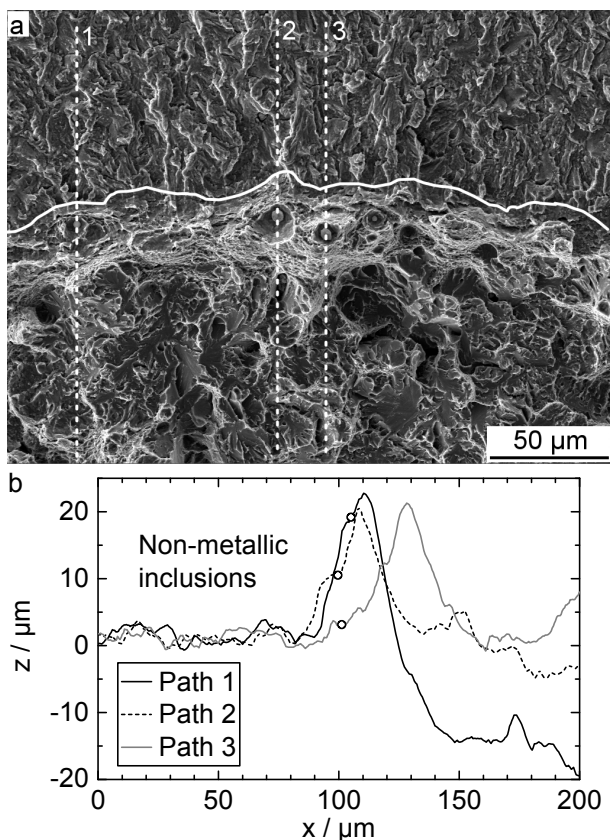


**Fig. 7.** Crack tip blunting is affected by non-metallic inclusions: (a) fracture surface, (b) height profiles along the paths given in subfigure a.  $T = -40\text{ }^{\circ}\text{C}$ .

it is assumed that further reduction in temperature is necessary to promote cleavage fracture.

Crack tip blunting was quantitatively investigated. The fracture surface in Figure 7a exhibits non-metallic inclusions which were located near the original crack tip. Figure 7b shows the effect of these non-metallic inclusions on the crack tip blunting. It was observed that the amount of blunting was lowest if the non-metallic inclusions were located at a small distance in front of the precrack tip (paths 1 and 2). Furthermore, even relatively large non-metallic inclusions, like the ones at paths 2 and 3 (5–6 micrometers in diameter), did not act as cleavage crack initiators.

From the topography measurements, the crack tip blunting in terms of stretch zone width (SZW) and stretch zone height (SZH) at different temperatures can be determined. It was found that both SZW and SZH decreased with decreasing temperature. Hence, the microscopic toughness qualitatively reflects the temperature dependency of  $J_{di}$ . However, the average values of both SZW and SZH decreased by 28% and 36%, respectively. This discrepancy was attributed to the scatter which is typically observed when characterizing the stretch zone in terms of SZW and SZH.

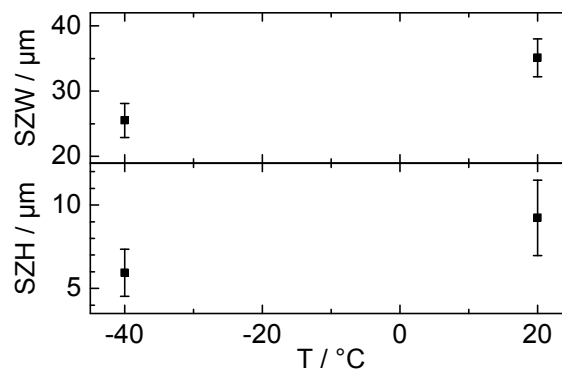


**Fig. 8.** Average and standard deviation of SZW and SZH for different temperatures.

## 4 Summary and Conclusions

The onset of stable crack growth was determined at a loading rate of approximately  $2 \cdot 10^6 \text{ MPa } \sqrt{\text{m}} \text{ s}^{-1}$  and at temperatures of  $20\text{ }^{\circ}\text{C}$  and  $-40\text{ }^{\circ}\text{C}$ . Force measurements by strain gauges at the bars and at the specimen were applied in combination with high-speed photography in order to detect the onset of crack growth. The main conclusions can be drawn as follows:

- By applying a pulse shaper, force equilibrium was achieved at low loads prior to the onset of crack extension.
- Irrespective of the temperature, the steel 42CrMo4 exhibited crack tip blunting followed by stable crack growth. The amount of blunting of the precrack and the ductile fracture was affected by the spacial distribution of non-metallic inclusions.
- Non-metallic inclusions caused strain localization and crack path deflection.
- The J Integral at the point of dynamic crack initiation decreased by 50% by decreasing the temperature from  $20\text{ }^{\circ}\text{C}$  to  $-40\text{ }^{\circ}\text{C}$ .
- The amount of blunting was reduced with decreasing temperature.
- At  $T = -40\text{ }^{\circ}\text{C}$ , the crack started to grow in a ductile manner. After short stable crack extension, cleavage fracture was observed. The change in crack growth mechanism was not quantified yet.

The authors thank the German Research Foundation (DFG) for its financial support of the investigations at the Collaborative Research Center 920, subproject C05. The support of Annette Ludwig and Gerd Schade during the experimental work is greatly appreciated.

## References

1. W.W. Chen, B. Song, eds., *Split Hopkinson (Kolsky) bar: Design, testing and applications* (Springer, New York, 2011)
2. F. Jiang, K.S. Vecchio, *Metall. Mater. Trans. A* **38**, 2896 (2007)

3. J.T. Foster, W.W. Chen, V.K. Luk, *Eng. Fract. Mech.* **78**, 1264 (2011)
4. D.J. Frew, M.J. Forrestal, W.W. Chen, *Exp. Mech.* **41**, 40 (2001)
5. T. Weerasooriya, P. Moy, D. Casem, M. Cheng, W.W. Chen, *J. Am. Ceram. Soc.* **89**, 990 (2006)
6. S. Henschel, D. Krewerth, F. Ballani, A. Weidner, L. Krüger, H. Biermann, M. Emmel, C.G. Aneziris, *Adv. Eng. Mater.* **15**, 1216 (2013)
7. S. Henschel, L. Krüger, *Fract. Struct. Integrity* **34**, 326 (2015)
8. J.R. Klepaczko, *J. Eng. Mater. Techn. (Trans. ASME)* **104**, 29 (1982)
9. J.R. Klepaczko, *Int. J. Impact Eng.* **3**, 191 (1985)
10. S. Henschel, L. Krüger, *EPJ Web of Conferences* **94**, 01028 (2015)
11. S. Henschel, L. Krüger, *Int. J. Fract.* **201**, 235 (2016)
12. A. Krabiell, W. Dahl, *Influence of strain rate and temperature on the tensile and fracture properties of structural steels*, in *Proceedings of 5th International Conference on Fracture*, edited by D. François (Pergamon, Oxford, 1982), pp. 393–400
13. J.F. Kalthoff, S. Winkler, W. Böhme, *J. Phys. Colloques* **46**, 179 (1985)
14. *ISO 26843* (2015), Metallic materials – Measurement of fracture toughness at impact loading rates using precracked Charpy-type test pieces
15. *ASTM E 1820* (2015), Standard test method for measurement of fracture toughness
16. *DIN EN ISO 148-1* (2017), Metallische Werkstoffe – Kerbschlagbiegeversuch nach Charpy – Teil 1: Prüfverfahren
17. G.T. Gray, in *ASM Handbook*, edited by H. Kuhn, D. Medlin (ASM International, Ohio, 2000), Vol. 8, pp. 462–476
18. S. Henschel, L. Krüger, *Eng. Fract. Mech.* **133**, 62 (2015)
19. *ASTM C 1421* (2010), Standard test methods for determination of fracture toughness of advanced ceramics at ambient temperature
20. A. Weidner, T. Mottitschka, H. Biermann, S. Henkel, *Eng. Fract. Mech.* **108**, 294 (2013)